



OPEN

Facile synthesis of silver doped manganese oxide nanocomposite with superior photocatalytic and antimicrobial activity under visible spectrum

Sherif Elbasuney^{1✉}, Ahmed M. El-Khawaga^{2✉}, Mohamed A. Elsayed³, Amir Elsaydy⁴, M. Yehia⁵ & Miguel A. Correa-Duarte⁵

Water pollution and antimicrobial resistance (AMR) have become two global threats; 80% of diseases and 50% of child deaths are due to poor water quality. In this study, hydrothermal processing was employed to manufacture manganese oxide nanorods. Silver dopant was deposited on the surface of manganese oxide. XRD diffractogram confirmed the facile synthesis of Ag/Mn₂O₃ nanocomposite. XPS survey analysis demonstrated silver content of 9.43 atom %. Photocatalytic measurements demonstrated the outstanding efficiency of the Ag-Mn₂O₃ compared to virgin oxide particles under visible radiation. Degradation efficiencies Mn₂O₃ and Ag/Mn₂O₃ on methyl orange (MO) dye was found to be 53% and 85% under visible spectrum. Silver dopant was found to decrease the binding energy of valence electrons; this action could support electron–hole pair generation under visible spectrum and could promote catalytic performance. Ag/Mn₂O₃ NPs demonstrated most effective performance (95% removal efficiency) at pH 3; this could be ascribed to the electrostatic attraction between positively charged catalyst and the negatively charged MO. Ag/Mn₂O₃ demonstrated enhanced antibacterial activity against Gram-positive *Staphylococcus aureus* (*S. aureus*) (19 mm ZOI), and Gram-negative *Escherichia coli* (*E. coli*) (22 mm ZOI) respectively; the developed nanocomposite demonstrated advanced anti-film activity with inhibition percentage of 95.5% against *E. coli* followed by 89.5% against *S. aureus*.

Keywords Nanoparticles, Photocatalysis, Water-treatment, Antimicrobial activity

The global scale of water purification has become an urgent concern due to modern industries and population growth. Recently, water pollution and antimicrobial resistance (AMR) have become two global threats^{1,2}. It has been reported that 80% of diseases and 50% of child deaths are due to poor water quality³. Approximately 17–20% of global pollutants can be attributed to the textile industry, according to the World Bank estimates⁴. The persistent nature of these pollutants stems from the stability of water-soluble Azo dyes; that would result in prolonged environmental impacts^{5,6}. Methyl Orange (MO) belongs to the azo dye family; it is known to be carcinogenic organic substance. MO is widely-used in paper manufacturing, pharmaceutical, food industries, and in research laboratories as an acid–base indicator^{7,8}. Direct contact with the eyes can result in chemical burns. When MO comes in contact with the skin, it may produce toxic effects. There is a significant interest towards advanced water treatment strategies, due to the extensive contamination of water resources⁹. The provision of un-contaminated water and the development of sustainable water purification methodologies are of paramount importance from industrial, societal, and environmental perspectives. The integrity of the natural ecosystem is being critically compromised due to the accelerated speed of global industrialization. Industrial discharge of

¹Head of Nanotechnology Research Center, Military Technical College, Cairo, Egypt. ²Department of Basic Medical Sciences, Faculty of Medicine, Galala University, New Galala City 43511, Suez, Egypt. ³Head of School of Chemical Engineering, Military Technical College, Cairo, Egypt. ⁴School of Chemical Engineering, Military Technical College, Cairo, Egypt. ⁵Biomedical Research Center (CINBIO), and Institute of Biomedical Research of Ourense-Pontevedra-Vigo (IBI), Universidad de Vigo, 36310 Vigo, Spain. ✉email: sherif_basuney2000@yahoo.com; s.elbasuney@mtc.edu.eg; Ahmed.Elkhawaga@gu.edu.eg; Ahmedelkhawaga15@gmail.com

hazardous dyes exposes detrimental effects on the environment. Conventional treatment methods that rely on centralized systems are no longer sustainable.

In recent years, the problem of bacteria antibiotic resistance to traditional antibiotics has reached a critical level¹⁰. The world population would be facing a real possibility of post-antibiotic era, where common infections and minor injuries could become life-threatening. According to World Health Organization, anti-microbial resistance, is expected to withstand the death of one person every three seconds, by 2050¹¹. Traditional approaches to water treatment like coagulation, flocculation¹², sedimentation¹³, and filtration¹⁴, have been employed. However, these methods often fall short in terms of efficiency, cost-effectiveness, and environmental impact. The utilization of nanomaterials in photocatalytic processes for treatment of harmful textile dyes has been identified as an environmentally friendly approach. The distinctive characteristics of photocatalytic nanomaterials experienced a significant impact on textile dye treatment¹⁵. Nanotechnology has been applied as a prominent approach for waste-water treatment¹⁶. NPs experienced superior physical and biological reactivity owing to their high interfacial surface area. Enhanced adsorption and photocatalytic activities of NPs could secure new sustainable solution for waste-water treatment. Semiconductors are of interest due to low cost, high physical and chemical stability, with minimum toxicity. However, the wide band-gap energy limits the photocatalytic applications to only 5% of the entire solar spectrum. Doping with rare earth elements was found to enhance the photocatalytic activities of semiconductors. Therefore, the NP band-gap value can be adjusted by controlling the size without altering their chemical composition. Narrow band-gap matching with the visible light absorption is highly appreciated for advanced photocatalyst. Extensive research has been conducted on metal oxides to enhance their functionality and to investigate their exceptional physical properties^{17–19}. Many metal-based catalysts are only active under ultraviolet irradiation, which accounts for just 5% of solar radiation; this action could impose the use of high-energy consumption Xenon or UV lamps. Manganese oxides (Mn_xO_x) can offer different oxidation states; manganese oxide has been investigated as effective photocatalyst for organic pollutants degradation. Manganese oxide is favored for simple production processes, low cost, low toxicity, high adsorption, and oxidation capabilities. Various studies have been conducted on Mn_xO_x -based photocatalysts to remove aquatic pollutants due to their large specific surface area and excellent adsorption properties^{20,21}. Silver in its free ionic form is highly toxic to human cells. It has been demonstrated that doping with silver on metal oxide eliminated silver ion toxicity to human cells. Additionally, doping with silver can inherit metal oxide particles superior antibacterial activity²².

Manganese oxide with consistent product quality has been developed; doping with silver on oxide lattice could be useful. It has been reported that doped manganese oxides materials experienced good catalytic activity²³. This study reports on the facile synthesis of colloidal manganese oxide nanorods via hydrothermal synthesis. The potential impact of silver dopant on adsorption capabilities, and photocatalytic activity was assessed to virgin manganese oxide. The potential impact of silver on antimicrobial and anti-biofilm activities against some pathogenic microbes was assessed to be virgin manganese oxide. This study shed light on the facile development of narrative cost effective, photocatalyst for wastewater treatment.

Materials and methods

Chemicals

Manganese nitrate (99%, Aldrich) was employed as the precursor for Mn_2O_3 synthesis. Hydrogen peroxide (30 V %, Aldrich) was employed as a source for OH^- ion. Methyl Orange (MO) obtained from Aldrich (Aldrich, purity < 100%), was employed as a contaminant. Ultrapure milli-Q water was employed as the water source. Silver nitrate (99%, Aldrich) was employed as a precursor for silver deposition. All chemicals were utilized without undergoing additional purification procedures.

Manganese oxide synthesis

Manganese oxide nanorods were fabricated in a continuous manner via hydrothermal processing. Manganese metal salt flow (B) was immediately mixed with supercritical water (ScW) flow (A). Manganese oxide nanorods were continuously produced in the reactor (R) at the boundary of the two fluids. Flow (A) was 20 ml/min supercritical water at 400 °C and 240 bars. Flow (B) was 0.05 M manganese nitrate at 10 ml/min, 25 °C and 240 bars (Supplementary Figure S1). Further details about the hydrothermal processing of various forms of manganese-oxides can be found in the following reference^{24,25}.

Ag/ Mn_2O_3 synthesis

Manganese oxide particles were dispersed in silver nitrate solution using an ultrasonic bath for 1 h. The weight percentage of Mn_2O_3 to silver ion was 9:1. Subsequently, silver deposition was conducted under strong magnetic stirring using sodium borohydride; the stoichiometric ratio of sodium borohydride to silver ion was 3:1. This approach could secure optimal homogeneity and even silver deposition on Mn_2O_3 surface.

Characterization of catalyst NPs

Transmission Electron Microscope (TEM) (JEM-HR-2100, Joel Corporation) and Scan Electron Microscope (SEM) (Zeiss EVO-10, Carl Zeiss Corporation) were used to study the morphological structure of manufactured Mn_2O_3 nanorods. The crystalline phase of manganese oxide was examined using XRD D8 advanced by Burker Corporation. The elemental composition of silver doped manganese oxide, and binding energy of valence electron were examined using an X-ray photoelectron spectroscopy XPS/ESCA equipment.

Photocatalytic performance of Ag/ Mn_2O_3 against methyl orange

A nanocomposite catalyst (10 mg) was introduced into 50 ml aqueous solution containing methyl orange (MO), with an initial concentration (C_0) of 10 mg/L. The mixture was stirred continuously at room temperature (25 °C)

for 30 min in the absence of light to establish equilibrium between adsorption and desorption processes. Subsequently, a simulated UV light source in the form of UV lamp was employed to illuminate the solution containing the photocatalyst and MO. The UV lamp was positioned axially within a quartz immersion tube. At fixed time intervals, a syringe equipped with a filter (pore size of 0.22 μm) was employed to extract a 1 ml sample of the MO suspension. The degradation rate of MO was determined by assessing the change in MO concentration over the course of irradiation time using a UV–visible spectrophotometer (Agilent Technologies Cary 60 UV–visible) at a wavelength (λ_{max}) of 464 nm. Deionized water served as the reference medium²⁶.

Antimicrobial activity and minimal inhibitory concentration (MIC)

The antimicrobial efficacy of the virgin Mn_2O_3 and $\text{Ag}/\text{Mn}_2\text{O}_3$ was assessed using the agar–disc diffusion method²⁷ against both Gram–negative (*Escherichia coli* ATCC 25922), and Gram–positive (*Staphylococcus aureus* ATCC 25923) bacteria. For performance comparison, conventional antibiotic discs containing gentamycin (CN) at a concentration of 10 $\mu\text{g}/\text{disc}$ and with a diameter of 6.0 mm were employed alongside the nanoparticle under investigation.

The minimum inhibitory concentrations (MIC) of the potent antimicrobial samples were determined using the serial dilution technique within a Luria–Bertani (LB) medium²⁸. This procedure involved the utilization of negative controls, which included the medium broth, as well as positive controls represented by the target pathogenic microorganisms along with the medium broth. The synthesized nanoparticle (initial concentration from 20.0 $\mu\text{g}/\text{ml}$ to 0.625 $\mu\text{g}/\text{ml}$) were included in the assessment. Following that, the inoculum of the examined bacteria and yeast was set to a concentration of 0.5 McFarland. The MIC values were ascertained after a 24 h incubation period at a temperature of 36.0 ± 1.0 °C²⁹. MIC was defined by using the ELISA plate method after setting the fixed wavelength at 600 nm³⁰. The MIC was described as the lowest concentration of the virgin Mn_2O_3 and $\text{Ag}/\text{Mn}_2\text{O}_3$ that inhibits 99.0% of the growth of the tested bacteria.

Antibiofilm activity of synthesized nanoparticles

Qualitative assessment regarding the inhibition of biofilm formation was conducted, via the methodology outlined by Christensen et al.³¹. Comprehensive examination of biofilm formation was carried out within the inner surface of test tubes, both in the absence and presence of $\text{Ag}/\text{Mn}_2\text{O}_3$ NPs. The anti–biofilm properties of $\text{Ag}/\text{Mn}_2\text{O}_3$ NPs at a concentration of 10.0 $\mu\text{g}/\text{mL}$ were assessed and compared to a control group (untreated). Nutrient broth medium (5 mL) was introduced into all tubes, followed by the inoculation of the test bacteria. That was adjusted to a concentration of $1\text{--}3.5 \times 10^8$ colony–forming units per milliliter (CFU/mL) equivalent to 0.5 McFarland standardization. Subsequently, they were incubated at 37.0 ± 0.5 °C for 24 h. The media from both the control and treated tubes were discharged; subsequently the tube was filled with phosphate buffer saline (PBS) at pH 7.0. The bacterial cells adhered to the tube walls were dislodged by treating with 5 mL of 3.5% sodium acetate for approximately 20 min, followed by a thorough cleaning with de–ionized water. The biofilms formed inside the tubes were stained with 20 mL of 0.15% Crystal Violet (CV) and subsequently rinsed with de–ionized water to remove excess CV. It is noteworthy that for semi–quantitative assessment of antibiofilm activity, 5 mL of absolute ethanol was introduced to dissolve the stained bacterial biofilms³². The optical density (O.D.) of the stained bacterial biofilms was measured using a UV–Vis spectrophotometer at 570.0 nm³³. The inhibition percentage of bacterial biofilm formation was calculated using Eq. 1³⁴:

$$\text{Biofilm inhibition\%} = \left[\frac{(\text{O.D. Control sample} - \text{O.D. treated sample})}{\text{O.D. Control sample}} \right] \times 100 \quad (1)$$

Results and discussion

Characterization of nanocatalyst

$\text{Ag}/\text{Mn}_2\text{O}_3$ demonstrated nanorods of 500 nm length and 20 nm diameters. High quality particles were assessed via TEM micrographs as represented in Fig. 1.

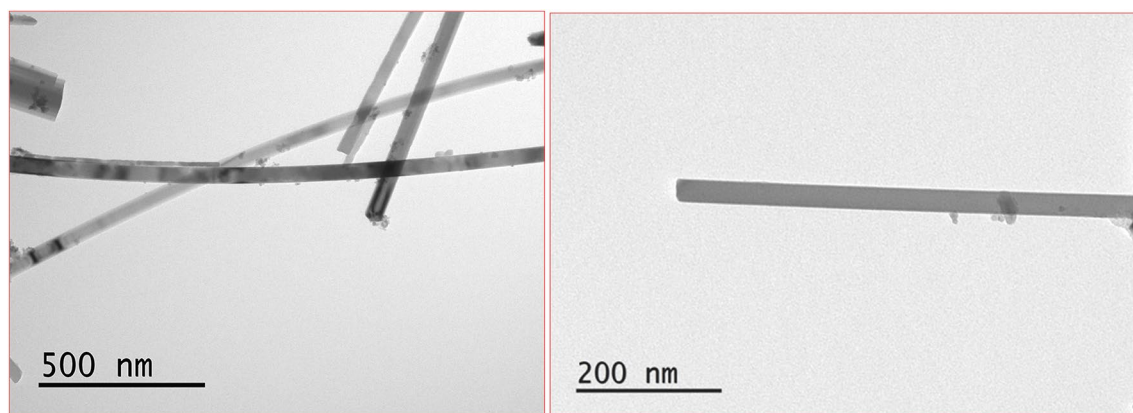


Figure 1. TEM micrographs of $\text{Ag}/\text{Mn}_2\text{O}_3$ nanorods.

XRD diffractogram of synthesized Mn_2O_3 demonstrated crystalline structure with 6 sharp peaks at $2\theta = 32.95, 38.24, 45.18, 49.35, 55.19, 65.81$ corresponding to (222), (400), (323), (431), (440), (622) planes respectively. XRD diffractogram of synthesized $\text{Ag}/\text{Mn}_2\text{O}_3$ confirmed the proper deposition of silver nanocatalyst on the surface of Mn_2O_3 . Silver particles demonstrated characteristic sharp peaks at $2\theta = 38.11, 44.27, 64.42, 77.47$ corresponding to (1,1,1), (2,0,0), (2,2,0), and (3,1,1) respectively (Fig. 2).

Average crystallite size of Mn_2O_3 NPs was further evaluated using Debye-Scherrer Eq. (2) via the major diffraction peak³⁵.

$$D = \frac{K\lambda}{\beta \cos\theta} \quad (2)$$

where k is a constant equal to 0.94, λ is the wavelength, β is the full width at half maximum height (FWHM) of the diffraction peak in radians, and θ is the Bragg angles of the main planes. Crystallite size evaluation was found to be in good agreement with TEM micrographs. SEM micrographs demonstrated a great tendency to aggregate on drying. Elemental mapping confirmed the uniform dispersion of silver on the surface of Mn_2O_3 NPs (Figure S2). Elemental composition was investigated using XPS analysis. Atomic ratios were computed from peak intensity. Survey composition of $\text{Ag}/\text{Mn}_2\text{O}_3$ was verified to virgin Mn_2O_3 is represented in Fig. 3.

Elemental survey confirmed the proper deposition of elemental silver element. Elemental composition of $\text{Ag}/\text{Mn}_2\text{O}_3$ was evaluated to virgin Mn_2O_3 (Table 1).

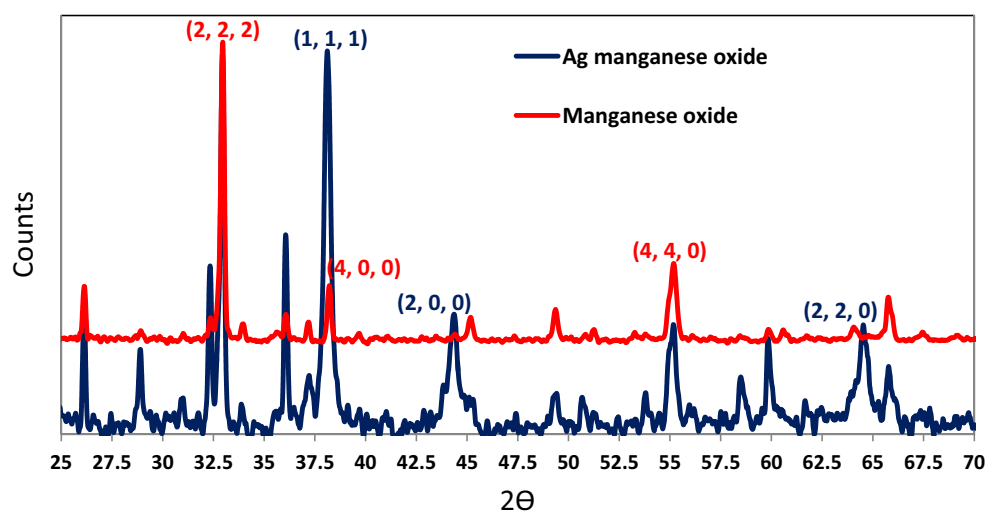


Figure 2. XRD of synthesized $\text{Ag}/\text{Mn}_2\text{O}_3$.

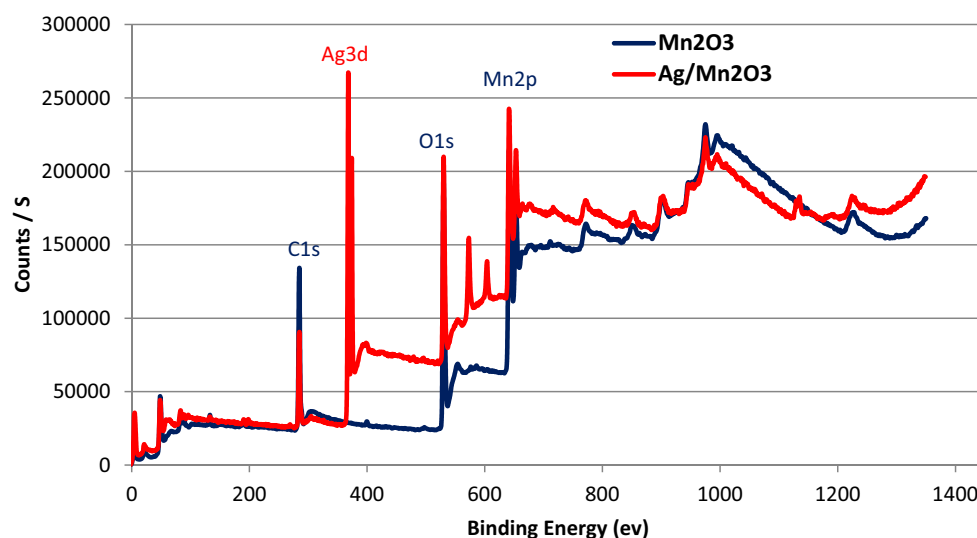


Figure 3. Survey of elemental composition of $\text{Ag}/\text{Mn}_2\text{O}_3$ to virgin Mn_2O_3 .

XPS elemental atomic percentage (At. %)					
Sample	C1s	O1s	Mn _{2p}	Others	Ag3d
Mn ₂ O ₃	50.58	35.88	9.67	3.87	--
Ag/Mn ₂ O ₃	39.24	37.43	11.65	2.25	9.43

Table 1. Elemental composition of Ag/Mn₂O₃ to Mn₂O₃ using XPS spectroscopy.

Elemental composition confirmed the successful deposition of silver on the surface of Mn₂O₃ particles. Silver dopant was found to have a significant impact on binding energy (BE) of surface oxygen; silver dopant offered low binding energy of surface oxygen. Therefore, surface oxygen electrons could be involved more effectively into catalytic reactions. The impact of silver dopant on O1s binding energy is demonstrated in Fig. 4.

Silver dopant was found to enhance the content of O1s A, with low BE; this was accomplished on the extent of O1s B and C with high BE (Table 2).

Furthermore, silver dopant was found to decrease the binding energy of Mn 3S electrons, via the increase of Mn3s A (with low BE) on the extent on Mn3S B (with high BE) (Fig. 5).

Silver dopant was found to increase the atomic percent of Mn3 s A (with low BE) on the extent of Mn3 s B (with high BE) (Table 3).

XPS spectrum of silver dopant confirmed the proper deposition of elemental silver. Ag 3d envelope is represented in Fig. 6.

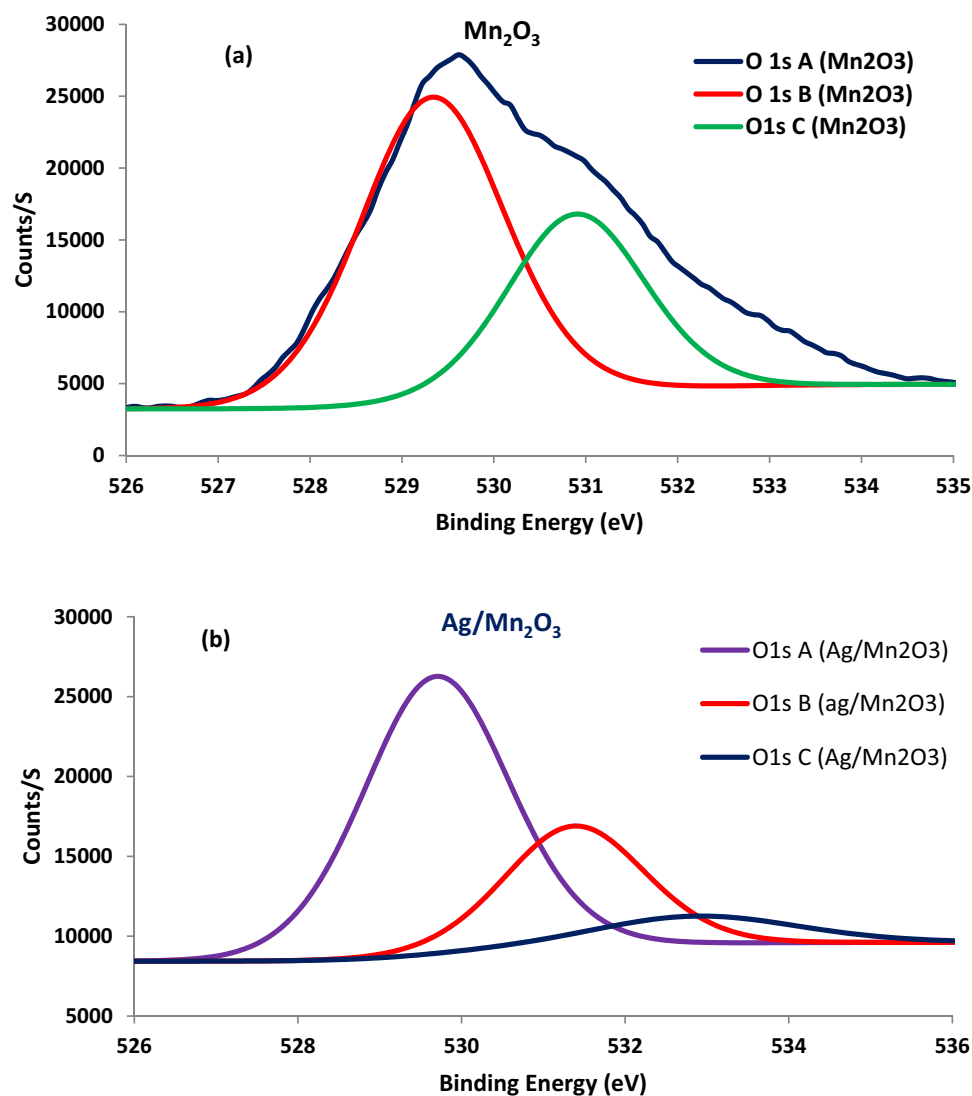


Figure 4. The impact of silver dopant on the binding energy of surface oxygen electrons (O1s).

Name	B.E	Mn ₂ O ₃	Ag/Mn ₂ O ₃
		Atomic %	Atomic %
O 1s A	529.33	55.14	64.26
O 1s B	530.9	30.64	26.89
O 1s C	532.5	14.22	8.85

Table 2. The impact of silver dopant on binding energy of O1 S.

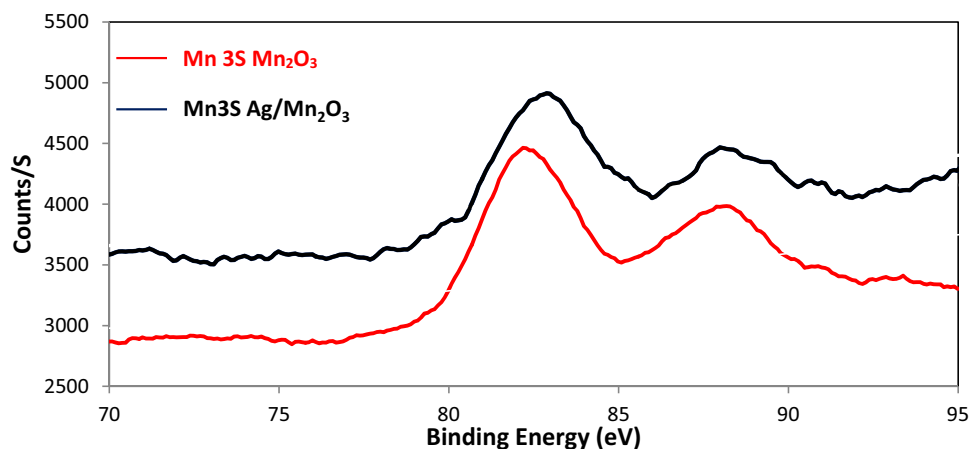


Figure 5. The impact of silver dopant on Mn 3S binding Energy.

Name	B.E	Mn ₂ O ₃	Ag/Mn ₂ O ₃
		Atomic %	Atomic %
Mn3 s A	82.8	64.68	74.14
Mn3 s B	88.34	35.32	25.86

Table 3. The impact of silver dopant on binding energy of O1 S.

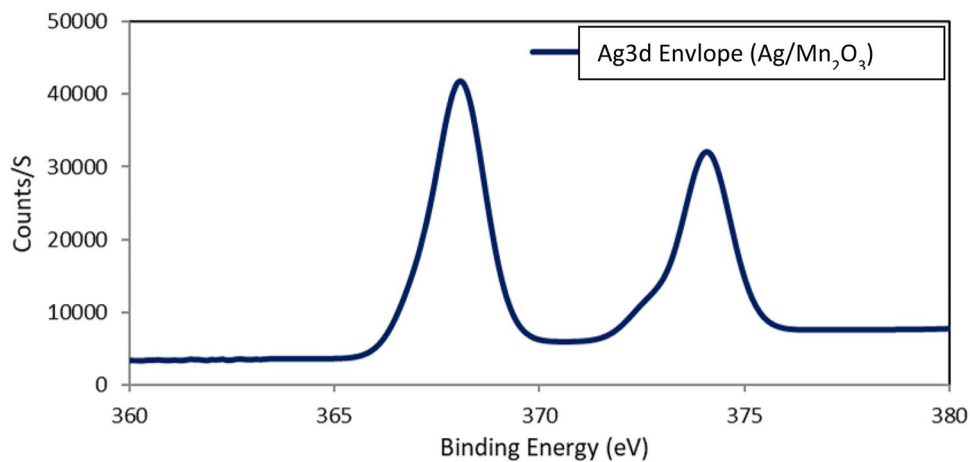


Figure 6. Binding Energy of Ag 3d silver dopant.

It is obvious that elemental silver was successfully deposited on the surface of Mn_2O_3 particles.

Photocatalytic performance of $\text{Ag}/\text{Mn}_2\text{O}_3$ NPs

The removal of MO was monitored at optimum absorbance wavelength, $\lambda_{\text{max}} = 464 \text{ nm}$ ³⁶. The UV–Vis spectrum of MO (10 ppm), and absorbance-concentration calibration curve is represented in Fig. 7.

The removal efficiency due to adsorption (in the absence of light) during the 135 min was approximately 34 and 38% for Mn_2O_3 and $\text{Ag}/\text{Mn}_2\text{O}_3$, respectively. On the other hand, the photocatalytic degradation of MO under UV light by Mn_2O_3 and $\text{Ag}/\text{Mn}_2\text{O}_3$ nanocatalyst reached 52 and 70%, respectively after 135 (Fig. 8b). The main finding in this study is that the photocatalytic performances of $\text{Ag}/\text{Mn}_2\text{O}_3$ nanocatalyst under visible light reached 85%, compared with 53% of Mn_2O_3 (Fig. 8c).

The superior photo-catalytic performance of $\text{Ag}/\text{Mn}_2\text{O}_3$ could be attributed to the presence of a metal–semiconductor hetero-junction within the nanocomposite; that could promote effective charge separation and light absorption.

Effect of pH on MO removal

The dependence of removal efficiency on solution pH was assessed. The influence of initial pH values was conducted under specified conditions (10 mg of the prepared nanocomposite, 50 ml of a 10 mg/L MO solution, temperature maintained at 25 °C); the experiment time was 90 min. Graphical representation could assess the variation in MO removal (%) over time at different solution pH levels (3.0, 5.0, 7.0, and 9.0). The maximum MO removal at equilibrium was observed at pH 3.0 (Fig. 9a). The point of zero charge (PZC) of the $\text{Ag}/\text{Mn}_2\text{O}_3$ nanocomposite was determined; 0.01 g of $\text{Ag}/\text{Mn}_2\text{O}_3$ nanocomposite was introduced into 50 mL of a 0.01 M NaCl solution. The pH of the solutions was adjusted to achieve pH values of 3, 5, 7, and 9. Subsequently, the samples were stirred at 200 rpm for 48 h, and pH measurements were conducted after the magnetic separation of $\text{Ag}/\text{Mn}_2\text{O}_3$ NPs. The pH value corresponding to the Point of Zero Charge (PZC) was determined by constructing a plot illustrating the final pH against the initial pH (Fig. 9b). The PZC pH point was identified as the pH value where no substantial disparity existed between the final and initial pH values. When the solution's pH matches the PZC pH, the surface charge of the photocatalyst becomes neutral; this could result in negligible electrostatic forces between the photocatalyst surface and ions (such as MO ions). The surface charge of the photocatalyst $\text{Ag}/\text{Mn}_2\text{O}_3$ becomes positive, when the pH is less than the PZC. The surface of photocatalyst becomes negative, when the pH exceeds the PZC.

The PZC pH for $\text{Ag}/\text{Mn}_2\text{O}_3$ NPs was calculated to be 6.2. This explains why the photocatalytic degradation of MO was most effective at pH 3.0 (Fig. 9a). At this pH, the net surface charge of $\text{Ag}/\text{Mn}_2\text{O}_3$ NPs is positive, resulting in attraction between the positively charged catalyst and the negatively charged MO; this action could offer enhanced photocatalytic efficiency.

Effect of initial concentration of MO

As the initial concentration of MO could play a pivotal role in the removal efficiency. The variation in removal percentage over time at different initial MO concentrations (5.0, 10.0, and 15.0 ppm) is represented in Fig. 10. The results revealed an inverse relationship between degradation efficiency with MO concentration.

Effect of the nanocomposite dose on degradation efficiency

The influence of a nanocomposite dose on MO removal efficiency under visible-light was investigated via different photocatalyst doses between 5 and 20 mg against a fixed concentration of MO (10 mg/l) (Fig. 11).

The results indicated an increase in removal efficiency with the increase in photocatalyst dose from (5–20 mg). It can be concluded that the maximum removal efficiency of MO was reached 95% at 20 mg of $\text{Ag}/\text{Mn}_2\text{O}_3$ NPs.

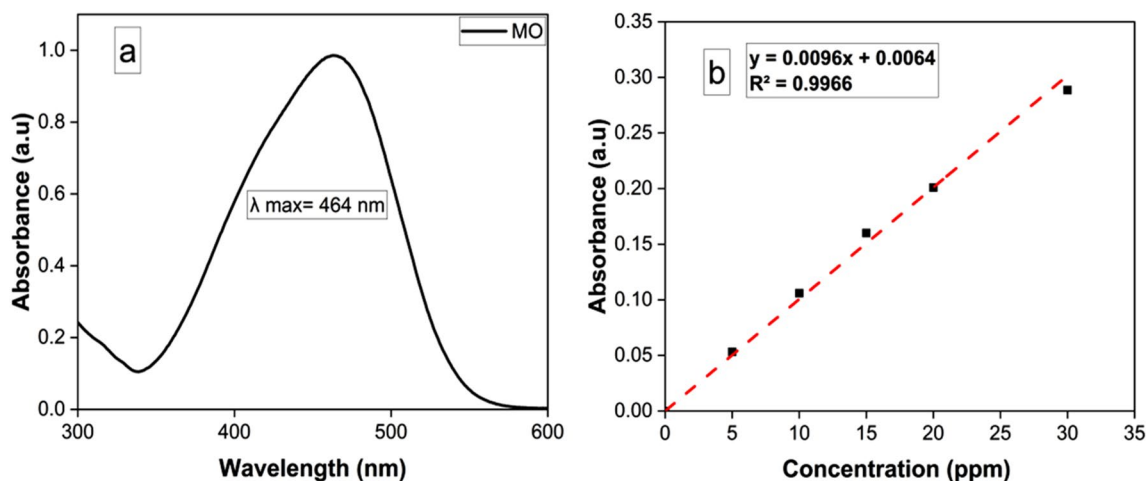


Figure 7. UV–Vis spectrum of MO (10 ppm) (a), Calibration curve of different concentrations of MO (b).

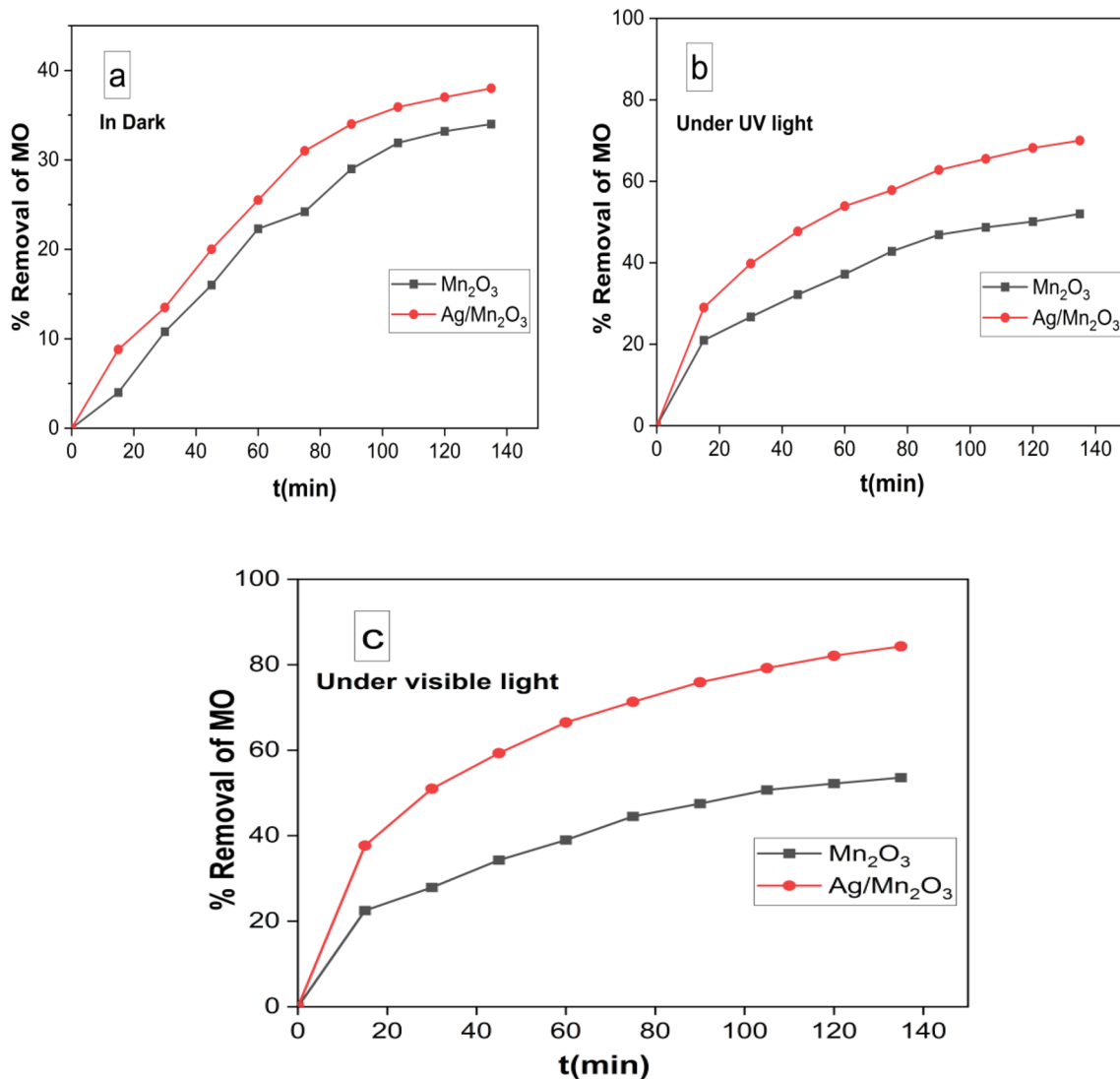


Figure 8. Removal % of MO via: adsorption in dark (a), Photocatalysis via UV irradiation (b), and photocatalysis under visible light irradiation (c).

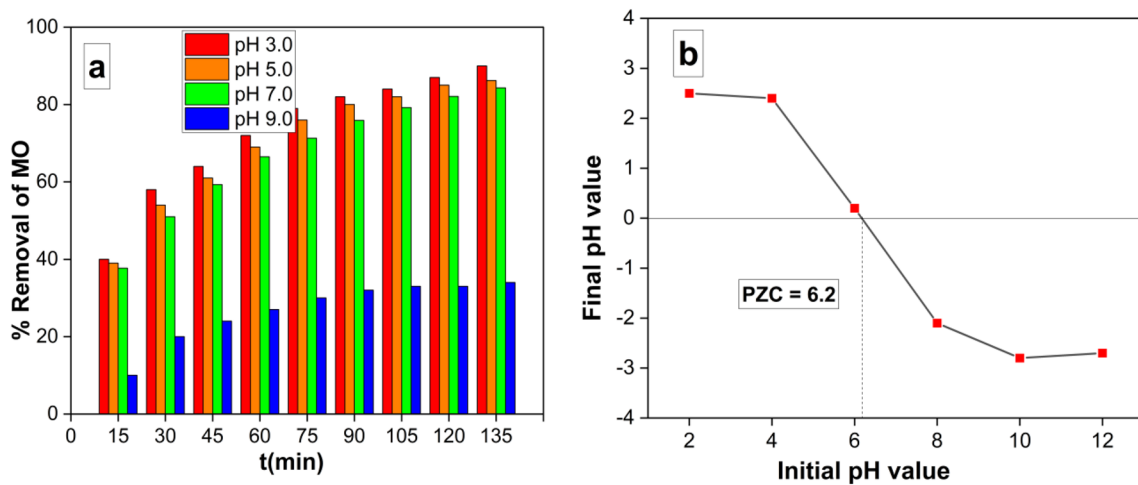


Figure 9. Showing the variation of MO removal (%) with time at different solution pH (3.0, 5.0, 7.0 and 9.0) (10 mg g of Ag/Mn₂O₃ NPs in 50 ml of 10 mg/l MO at 25 °C) (a), Point of zero charge (PZC) of Ag/Mn₂O₃ NPs at different pH values (b).

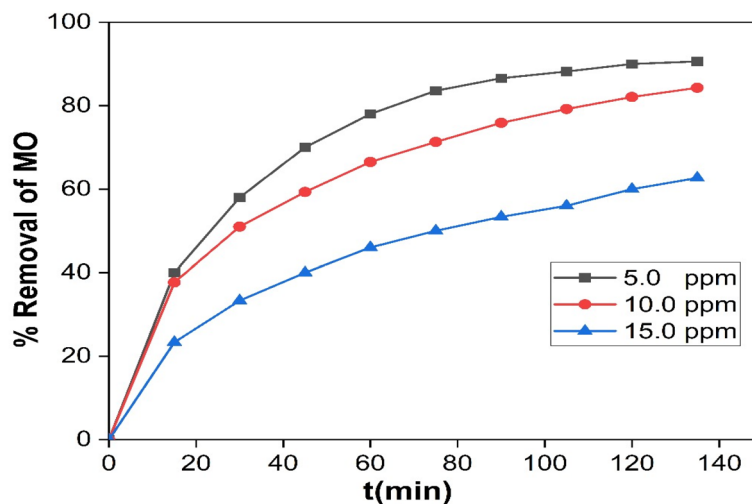


Figure 10. The variation of percent removal as a function of contact time at different initial MO concentration (5, 10 and 15 ppm) at pH 3.0 and 10.0 mg Ag/Mn₂O₃.

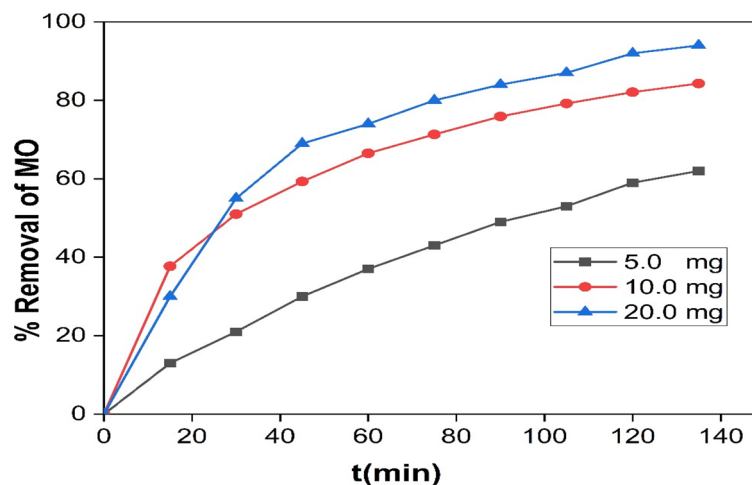


Figure 11. Effect of the photocatalyst dose on the Removal efficiency of MO (50 ml MO solution (10 mg/l), Temp. = 25 °C and pH 3.0).

The increase in removal efficiency with catalyst amount could be attributed to the increase in the available active area or active sites of the photocatalyst to volume ratio of MO solution³⁷.

Kinetic studies

The MO removal rate was computed using the following equation:

$$-\ln C_t/C_0 = -Kt \quad (3)$$

Here, C_t and C_0 denote for the remaining and initial concentrations of MO, respectively. The removal time is represented by t , and k represents the removal rate constant. The relationship between $-\ln(C_t/C_0)$ and t is represented in Fig. 12a. These findings indicated that the removal reaction kinetics adhered to pseudo-first-order rate. An augmentation in the MO initial concentration resulted in an increase in the apparent pseudo-first-order rate constants (Fig. 12b).

This dependency of reaction rate constants on MO concentration aligns well with previously reported literature³⁸. Pseudo-first-order kinetics could be a useful tool for initial analysis, it simplifies the photocatalytic degradation process. It assumes the reaction rate solely depends on the concentration of the pollutant (MO). In reality, other factors like light intensity, catalyst surface area, and mass transfer limitations can significantly impact the degradation rate. Photocatalysis involves multiple steps and interactions between light, catalyst, and pollutants. However, the pseudo-first-order model is a valuable tool for initial data analysis. In this study,

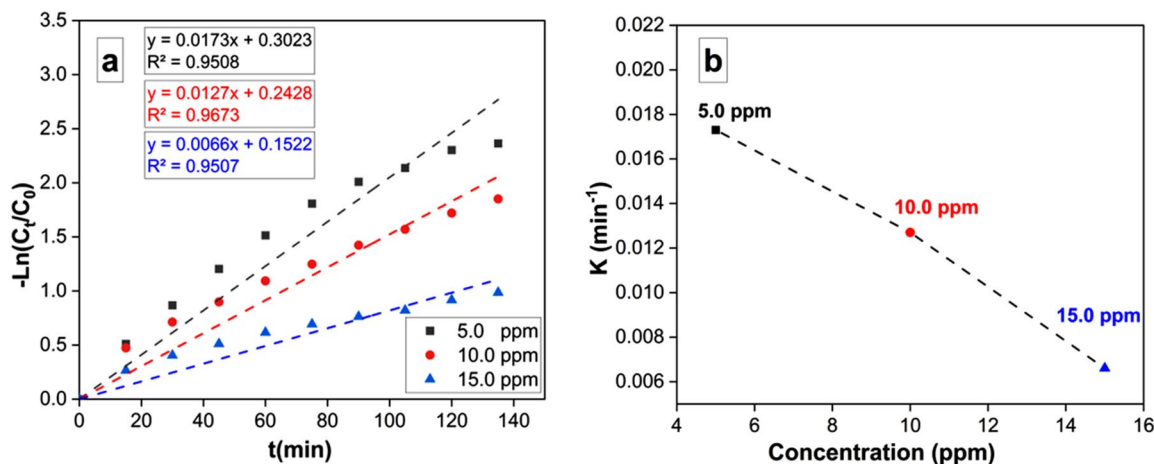


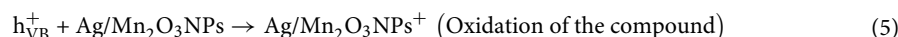
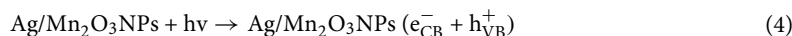
Figure 12. A linear fit, pseudo-first-order model data are reported in kinetic form for MO degradation under Visible-light irradiation with beginning MO concentrations of 5, 10, and 15 ppm.

pseudo-second-order kinetics might be a better fit because the adsorption of the pollutant onto the catalyst plays a significant role.

Mechanism of MO photocatalysis

The potential mechanism could be correlated to photodegradation mechanism, which is influenced by variations in pH values. Such mechanism encompasses the attack of hydroxyl radicals, with subsequent oxidation through the positive holes in the valence band, and reduction by the electrons in the conduction band. It is postulated that photocatalytic degradation is likely to occur due to the generation of electron–hole pairs on the surface of the employed photocatalyst induced by visible irradiation^{39,40}.

The oxidative potential of these holes may either react with -OH groups to form hydroxyl radicals or oxidize the reactive MO to generate a degradation product. The reactions involved in MO photocatalytic degradation can be summarized as follows (4–7).



Or



The suggested mechanism delineating the interaction between the prepared Ag/Mn₂O₃ NPs and MO is illustrated in Fig. 13. When Ag/Mn₂O₃ NPs are subjected to visible irradiation, the excitation process could generate charge carriers; that could initiate redox reactions. Consequently, the resultant free radicals, including OH· and O₂⁻ could participate in the degradation of MO, with the formation of smaller organic compounds. It is noteworthy that, as of the current stage, there have been no published reports regarding the degradation mechanism of MO.

Antimicrobial and antibiofilm activities of synthesized nanoparticles

Antimicrobial activity of synthesized Ag/Mn₂O₃ nanocatalyst

The in-vitro ZOI result verified that Ag/Mn₂O₃ NPs (20 μg/ml) exhibited enhanced antibacterial activity against *S. aureus* (19 mm ZOI), and *E. coli* (22 mm ZOI) respectively (Fig. 14).

The results demonstrated that the synthesized Ag/Mn₂O₃ NPs appeared more active towards the Gram-negative compared to that of Gram-positive bacteriological species. This may be due to structural and compositional variations between Gram-negative and Gram-positive bacterial cell walls⁷. Gram-positive bacteria have a dense coating of peptidoglycan to which teichuronic, and teichoic acids are covalently bound. However, Gram-negative bacteria have a thin coating of peptidoglycan with an exterior coating of negatively charged lipopolysaccharides⁸. Due to such reasons, the synthesized Ag/Mn₂O₃ NPs could expose significant inhibitory effect on Gram-negative than on Gram-positive bacterial species (Table 4).

Antibiofilm activity of Ag/Mn₂O₃ nanocatalyst

Biofilm generation has been recognized in several exopolysaccharide-forming microbes^{41,42}. Biofilm production by common pathogenic bacteria microorganisms in the absence and presence of Ag/Mn₂O₃ NPs was assessed

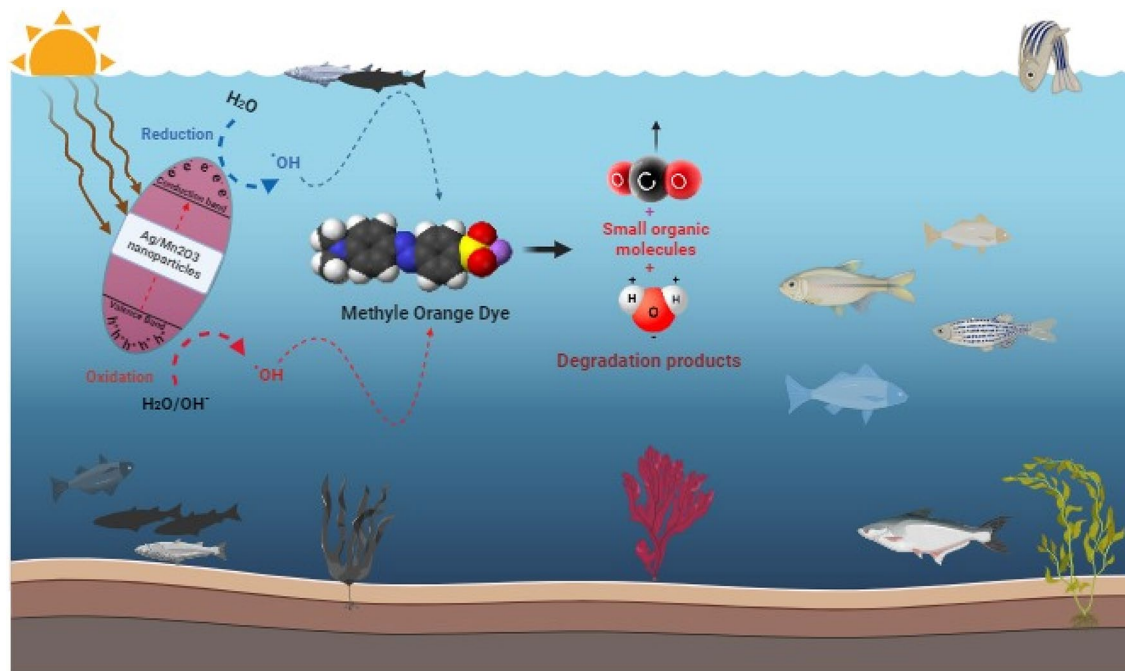


Figure 13. The possible photocatalytic reaction mechanism for MO photodegradation by Ag/Mn₂O₃ NPs.

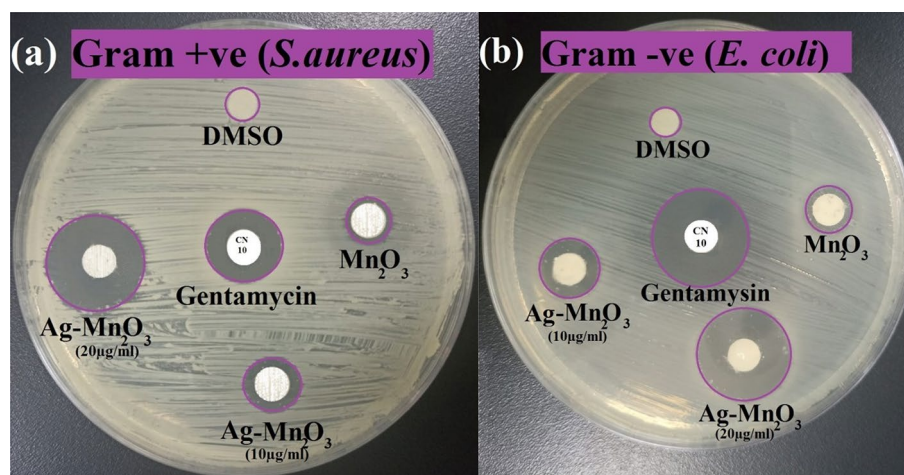


Figure 14. Antimicrobial activity of the synthesized NPs; Mn₂O₃, Ag/Mn₂O₃ (10 and 20 µg/ml), measured as ZOI (mm) against (a) gram positive *S. aureus*, (b) gram negative *E. coli*.

Bacterial Strains	ZOI of Mn ₂ O ₃ (10.0 µg/ml) (mm)	ZOI of Ag/Mn ₂ O ₃ (10.0 µg/ml) (mm)	ZOI of Ag/Mn ₂ O ₃ (20.0 µg/ml) (mm)	MIC of Ag/Mn ₂ O ₃ NPs (µg/ml)	CN	Antibiofilm (%)
<i>S. aureus</i>	7.0	9.0	19.0	2.50	14.0	89.5
<i>E. coli</i>	8.0	11.0	22.0	1.250	22.0	95.4

Table 4. Antimicrobial activities of Ag/Mn₂O₃, against gram-positive and gram-negative bacteria measured as ZOI (mm), MIC (µg/ml) and antibiofilm activity of Ag/Mn₂O₃.

using a test tube method⁴³. Figure 15a demonstrates the antibiofilm activity of Ag/Mn₂O₃ NPs against *E. coli* bacteria (as a model for susceptible bacteria). *E. coli* inoculated in the absence of Ag/Mn₂O₃ nanocomposite exhibited a thick whitish-yellow mat throughout the air-liquid interface. This mat was totally adhered to the wall of the test tubes and appeared as a blue ring after CV staining as displayed in Fig. 15b. A blue suspension was developed after dissolving the CV-stained ring with absolute ethanol, as displayed in Fig. 15c.

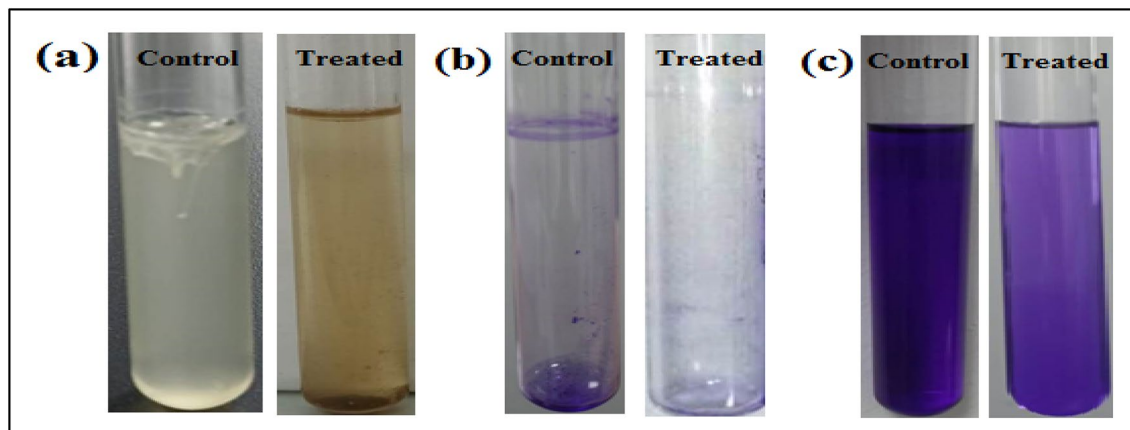


Figure 15. Antibiofilm activity of Ag/Mn₂O₃ NPs using the test tube method against *E. coli*. The steps were reported as follows. (a) Growth of the bacterial cells and biofilm formation (rings) without treatment with the synthesized Ag/Mn₂O₃ NPs and the inhibition of bacterial growth after treatment with Ag/Mn₂O₃ NPs. (b) Staining of the adherent bacterial cells with crystal violet. (c) Removing and dissolving the adherent bacterial and yeast cells by ethanol for determination of semi-quantitative biofilm inhibition (%) (Table 4).

On the other hand, *E. coli*-inoculated test tubes that were treated with Ag/Mn₂O₃ NPs (10.0 µg ml⁻¹), exhibited a suppressed effect where the development of bacterial rings was limited. In addition, the blue color representing CV-stained adherent bacterial cells was light and, after CV dissolution by ethanol, slightly blue color was observed (Fig. 15c). The optical density (at 570.0 nm) was determined after separating CV-stained bacterial biofilm with ethanol. Table 3 demonstrates the inhibition percentage of the biofilms formed by the tested bacteria. The highest inhibition percentage was observed against *E. coli* (95.5%; Fig. 16 and Table 4) followed by *S. aureus* (89.5%; Table 4) after treatment with 10.0 µg ml⁻¹ of Ag/Mn₂O₃ NPs. The synthesized Ag/Mn₂O₃ nanocatalyst was adopted to restrain the development of biofilm at its adhesion step (identified as the primary step). The variance in the percentage inhibition could be attributed to various circumstances, such as antimicrobial action, biosorption (because of the large surface area of the synthesized NPs), physical characteristics (particle size of the nanocomposite), invasion capabilities, and different chemical features that could control the interaction of the nanocomposite and the biofilms.

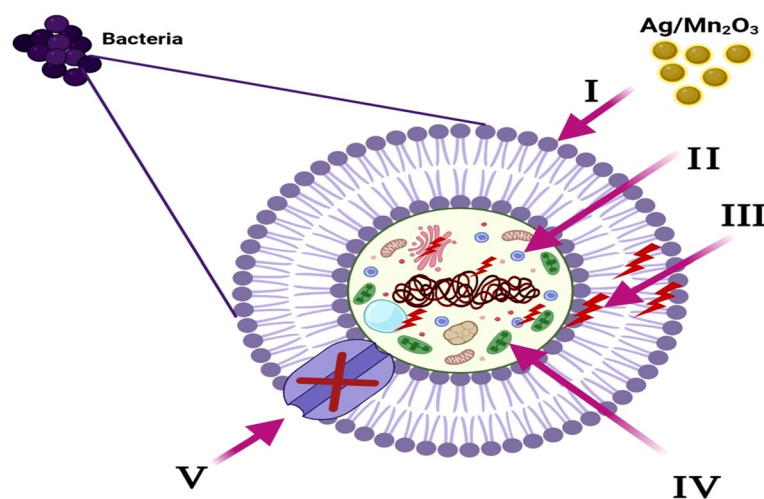


Figure 16. Schematic representation of the four main pathways underlying the antibacterial potential of the prepared Ag/Mn₂O₃ NPs: (I) The Ag/Mn₂O₃ NPs adhere to and wrap the microbial cell surface causing membrane damage and altered transport activity. (II) The prepared Ag/Mn₂O₃ NPs penetrate the microbial cells and interact with cellular organelles and biomolecules (such as plasmid DNA, ribosomes, chromosomal DNA, and mesosomes), affecting the respective cellular machinery. (III) The prepared Ag/Mn₂O₃ NPs create and increase ROS, leading to cell damage. (IV) Ag/Mn₂O₃ NPs modulate the cellular signal system and causing cell death. (V) Finally, Ag/Mn₂O₃ NPs nanocomposite blocks the ion transport from and to the microbial cells.

Mechanism of antimicrobial effect of the prepared Ag/Mn₂O₃ NPs

The antimicrobial mechanism of the prepared Ag/Mn₂O₃ NPs was proposed. The prepared Ag/Mn₂O₃ NPs begin their activity by wrapping and adhering at the exterior surface of the microbial cells, causing membrane destruction and changing the transport potential⁴⁴. Then, the distribution of the NPs inside the microbial cell divides all intracellular structures, including plasmid, DNA, and other essential organelles⁴⁵. Ultimately, cellular toxicity happens due to the oxidative stress created by the generation of ROS⁴⁶. Finally, nanocomposite blocks the ion transport from and to the microbial cells (Fig. 16).

Conclusion

Manganese oxide nanorods were prepared by hydrothermal processing. The developed Mn₂O₃ NPs were doped with silver. The photocatalytic efficiency of the prepared Ag-Mn₂O₃ was assessed against methyl orange dye. Degradation efficiencies Mn₂O₃ and Ag/Mn₂O₃ on methyl orange (MO) dye was found to be 53% and 85% under visible spectrum. Silver dopant was reported to decrease the binding energy of valence electrons; this action could support electron-hole pair generation under visible spectrum and could promote catalytic performance. Ag/Mn₂O₃ NPs demonstrated most effective performance (95% removal efficiency) at pH 3; this could be ascribed to the electrostatic attraction between positively charged catalyst and the negatively charged MO. Ag/Mn₂O₃ demonstrated enhanced antibacterial activity against *S. aureus* (19 mm ZOI), and *E. coli* (22 mm ZOI) respectively; the developed nanocomposite demonstrated advanced anti-film activity with inhibition percentage of 95.5% against *E. coli* followed by 89.5% against *S. aureus*.

Data availability

The data used to support the findings of this study are available from the corresponding author upon request.

Received: 4 May 2024; Accepted: 24 June 2024

Published online: 08 July 2024

References

- Song, Y., Phipps, J., Zhu, C. & Ma, S. Porous materials for water purification. *Angew. Chem. Int. Ed.* **62**, e202216724 (2023).
- Tian, M. *et al.* Pollution by antibiotics and antimicrobial resistance in livestock and poultry manure in china, and countermeasures. *Antibiotics* **10**, 539 (2021).
- Lin, L., Yang, H. & Xu, X. Effects of water pollution on human health and disease heterogeneity: A review. *Front. Environ. Sci.* **10**, 880246 (2022).
- Sahu, B. & Chopra, L. A review on removal of toxic colorants from the industrial effluent via advanced metal oxide semiconductor. In *AIP Conference Proceedings* **2535**. <https://doi.org/10.1063/5.0138202> (2023).
- Elbasuney, S. *et al.* Enhanced photocatalytic and antibacterial activities of novel Ag-HA bioceramic nanocatalyst for waste-water treatment. *Sci. Rep.* **7**, 46428–46439. <https://doi.org/10.1038/s41598-023-40970-4> (2023).
- Shaheen, F. *et al.* Size-controlled synthesis of La and chitosan doped cobalt selenide nanostructures for catalytic and antibacterial activity with molecular docking analysis. *Int. J. Biol. Macromol.* **263**, 130096. <https://doi.org/10.1016/j.ijbiomac.2024.130096> (2024).
- Khan, S. A. & Lee, C.-S. in *Applications of Nanotechnology for Green Synthesis* (eds Inamuddin & Abdullah M. Asiri) 247–280 (Springer International Publishing, 2020).
- Khan, S. A., Shahid, S. & Lee, C.-S. Green synthesis of gold and silver nanoparticles using leaf extract of *Clerodendrum inerme*; characterization, antimicrobial, and antioxidant activities. *Biomolecules* **10**, 835 (2020).
- Manikandan, S. *et al.* A critical review of advanced nanotechnology and hybrid membrane based water recycling, reuse, and wastewater treatment processes. *Chemosphere* **289**, 132867 (2022).
- Rani, S. *et al.* Dye degradation, antimicrobial activity, and molecular docking analysis of samarium-grafted carbon nitride doped-bismuth oxobromide quantum dots. *Glob. Chall.* **7**, 2300118. <https://doi.org/10.1002/gch2.202300118> (2023).
- Review on Antimicrobial, R. & Wellcome, T. *Tackling drug-resistant infections globally: final report and recommendations*. (Review on Antimicrobial Resistance, 2016).
- Zhao, C. *et al.* Application of coagulation/flocculation in oily wastewater treatment: A review. *Sci. Total Environ.* **765**, 142795 (2021).
- Culp, G., Hansen, S. & Richardson, G. High-rate sedimentation in water treatment works. *J. Am. Water Works Assoc.* **60**, 681–698 (1968).
- Cescon, A. & Jiang, J.-Q. Filtration process and alternative filter media material in water treatment. *Water* **12**, 3377 (2020).
- Tahir, M. B., Rafique, M., Sagir, M., Ullah, S. & Kiran, H. *Reference Module in Materials Science and Materials Engineering* (Elsevier, 2019).
- Saha, I. *et al.* Role of nanotechnology in water treatment and purification: Potential applications and implications. *Int. J. Chem. Sci. Technol.* **3**(3), 59–64 (2013).
- Chen, X., Zhou, Y., Roy, V. A. & Han, S. T. Evolutionary metal oxide clusters for novel applications: Toward high-density data storage in nonvolatile memories. *Adv. Mater.* **30**, 1703950 (2018).
- Qu, X., Alvarez, P. J. & Li, Q. Applications of nanotechnology in water and wastewater treatment. *Water Res.* **47**, 3931–3946 (2013).
- Abuzeyad, O. H., El-Khawaga, A. M., Tantawy, H. & Elsayed, M. A. An evaluation of the improved catalytic performance of rGO/GO-hybrid-nanomaterials in photocatalytic degradation and antibacterial activity processes for wastewater treatment: A review. *J. Mol. Struct.* **1288**, 135787 (2023).
- Cheng, Y., Zhang, Y., Xiong, W. & Huang, T. Simultaneous removal of tetracycline and manganese (II) ions from groundwater using manganese oxide filters: Efficiency and mechanisms. *J. Water Proc. Eng.* **42**, 102158 (2021).
- Song, Z., Ma, Y.-L. & Li, C.-E. The residual tetracycline in pharmaceutical wastewater was effectively removed by using MnO₂/graphene nanocomposite. *Sci. Total Environ.* **651**, 580–590 (2019).
- Kunkalekar, R. K., Naik, M. M., Dubey, S. K. & Salker, A. V. Antibacterial activity of silver-doped manganese dioxide nanoparticles on multidrug-resistant bacteria. *J. Chem. Technol. Biotechnol.* **88**, 873–877. <https://doi.org/10.1002/jctb.3915> (2013).
- Kunkalekar, R. K. & Salker, A. V. Low temperature carbon monoxide oxidation over nanosized silver doped manganese dioxide catalysts. *Catal. Commun.* **12**, 193–196. <https://doi.org/10.1016/j.catcom.2010.09.013> (2010).
- Elbasuney, S. Surface engineering of layered double hydroxide (LDH) nanoparticles for polymer flame retardancy. *Powder Technol.* **277**, 63–73 (2015).
- Elbasuney, S. Novel Colloidal Nanothermite Particles (MnO /Al) for Advanced Highly Energetic Systems. *J. Inorg. Organomet. Polym. Mater.* **28**, 1793–1800 (2018).

26. El-Khawaga, A. M., Farrag, A. A., Elsayed, M. A., El-Sayyad, G. S. & El-Batal, A. I. Promising antimicrobial and azo dye removal activities of citric acid-functionalized magnesium ferrite nanoparticles. *J. Clust. Sci.* **33**, 197–213. <https://doi.org/10.1007/s10876-020-01944-y> (2022).
27. Halarnekar, D. *et al.* Eco synthesized chitosan/zinc oxide nanocomposites as the next generation of nano-delivery for antibacterial, antioxidant, antidiabetic potential, and chronic wound repair. *Int. J. Biol. Macromol.* **242**, 124764 (2023).
28. Fei, P. *et al.* Antimicrobial activity and mechanism of action of olive oil polyphenols extract against *Cronobacter sakazakii*. *Food Control* **94**, 289–294 (2018).
29. Matouskova, P., Marova, I., Bokrova, J. & Benesova, P. Effect of encapsulation on antimicrobial activity of herbal extracts with lysozyme. *Food Technol. Biotechnol.* **54**, 304–316 (2016).
30. Abd Elkodous, M. *et al.* Therapeutic and diagnostic potential of nanomaterials for enhanced biomedical applications. *Colloids Surf. B Biointerfaces* **180**, 411–428 (2019).
31. Christensen, B. B. *et al.* Establishment of new genetic traits in a microbial biofilm community. *Appl. Environ. Microbiol.* **64**, 2247–2255 (1998).
32. El-Khawaga, A. M., Tantawy, H., Elsayed, M. A. & Abd El-Mageed, A. I. A. Synthesis and applicability of reduced graphene oxide/porphyrin nanocomposite as photocatalyst for waste water treatment and medical applications. *Sci. Rep.* **12**, 17075. <https://doi.org/10.1038/s41598-022-21360-8> (2022).
33. Mu, H. *et al.* Potent antibacterial nanoparticles against biofilm and intracellular bacteria. *Sci. Rep.* **6**, 18877 (2016).
34. Maksoud, M. I. A. A. *et al.* Antibacterial, antibiofilm, and photocatalytic activities of metals-substituted spinel cobalt ferrite nanoparticles. *Microb. Pathog.* **127**, 144–158. <https://doi.org/10.1016/j.micpath.2018.11.045> (2019).
35. Tillotson, T. *et al.* Sol–gel processing of energetic materials. *J. Non-Cryst. Solids* **225**, 358–363 (1998).
36. Tsai, F.-C. *et al.* Adsorptive removal of methyl orange from aqueous solution with crosslinking chitosan microspheres. *J. Water Proc. Eng.* **1**, 2–7. <https://doi.org/10.1016/j.jwpe.2014.02.001> (2014).
37. Mahmoodi, N. M. Photocatalytic ozonation of dyes using copper ferrite nanoparticle prepared by co-precipitation method. *Desalination* **279**, 332–337 (2011).
38. Ollis, D. F. Kinetics of photocatalyzed reactions: Five lessons learned. *Front. Chem.* **6**, 378 (2018).
39. Wang, D. *et al.* Photocatalytic degradation of organic dye and phytohormone by a Cu (II) complex powder catalyst with added H₂O₂. *Colloids Surf. A Physicochem. Eng. Asp.* **603**, 125147 (2020).
40. Harikishore, M., Sandhyarani, M., Venkateswarlu, K., Nellaippan, T. A. & Rameshbabu, N. Effect of Ag doping on antibacterial and photocatalytic activity of nanocrystalline TiO₂. *Proced. Mater. Sci.* **6**, 557–566 (2014).
41. Abraham, W.-R. Controlling biofilms of gram-positive pathogenic bacteria. *Curr. Med. Chem.* **13**, 1509–1524 (2006).
42. Arciola, C. R., Campoccia, D., Speziale, P., Montanaro, L. & Costerton, J. W. Biofilm formation in Staphylococcus implant infections. A review of molecular mechanisms and implications for biofilm-resistant materials. *Biomaterials* **33**, 5967–5982. <https://doi.org/10.1016/j.biomaterials.2012.05.031> (2012).
43. El-Sayyad, G. S. *et al.* Merits of photocatalytic and antimicrobial applications of gamma-irradiated CoxNi1-xFe2O4/SiO2/TiO2; x = 0.9 nanocomposite for pyridine removal and pathogenic bacteria/fungi disinfection: Implication for wastewater treatment. *RSC Adv.* **10**, 5241–5259. <https://doi.org/10.1039/C9RA10505K> (2020).
44. Maksoud, M. I. A. A. *et al.* Nanostructured Mg substituted Mn-Zn ferrites: A magnetic recyclable catalyst for outstanding photocatalytic and antimicrobial potentials. *J. Hazard. Mater.* **399**, 123000 (2020).
45. Ameen, M. T. *et al.* Exploring catalytic efficacy and anti-bacterial performance with molecular docking analysis of g-C₃N₄-grafted-Ag doped SnO₂ QDs. *Res. Chem. Intermed.* **50**, 1661–1678. <https://doi.org/10.1007/s11164-024-05241-5> (2024).
46. Ikram, M. *et al.* Experimental and computational study of annealed nickel sulfide quantum dots for catalytic and antibacterial activity. *Nano Mater. Sci.* <https://doi.org/10.1016/j.nanoms.2023.11.007> (2023).

Author contributions

S.E.: Conceptualization, data curation formal analysis, and writing—original draft. A.M.E.: Data curation, formal analysis, and writing—original draft. M.A.E.: Formal analysis and writing—original draft. A.E. and M.Y.: Formal analysis and writing—original draft., M.A.C.-D.: Writing—review—editing and supervision.

Funding

Open access funding provided by The Science, Technology & Innovation Funding Authority (STDF) in cooperation with The Egyptian Knowledge Bank (EKB).

Competing interests

The authors declare no competing interests.

Additional information

Supplementary Information The online version contains supplementary material available at <https://doi.org/10.1038/s41598-024-65749-z>.

Correspondence and requests for materials should be addressed to S.E. or A.M.E.-K.

Reprints and permissions information is available at www.nature.com/reprints.

Publisher's note Springer Nature remains neutral with regard to jurisdictional claims in published maps and institutional affiliations.



Open Access This article is licensed under a Creative Commons Attribution 4.0 International License, which permits use, sharing, adaptation, distribution and reproduction in any medium or format, as long as you give appropriate credit to the original author(s) and the source, provide a link to the Creative Commons licence, and indicate if changes were made. The images or other third party material in this article are included in the article's Creative Commons licence, unless indicated otherwise in a credit line to the material. If material is not included in the article's Creative Commons licence and your intended use is not permitted by statutory regulation or exceeds the permitted use, you will need to obtain permission directly from the copyright holder. To view a copy of this licence, visit <http://creativecommons.org/licenses/by/4.0/>.

© The Author(s) 2024